Detection of paramagnetic spins with an ultrathin van der Waals quantum sensor

Islay O. Robertson, ¹ Sam C. Scholten, ^{2,3} Priya Singh, ¹ Alexander J. Healey, ^{2,3} Fernando Meneses, ^{2,3} Philipp Reineck, ¹ Hiroshi Abe, ⁴ Takeshi Ohshima, ⁴ Mehran Kianinia, ^{5,6} Igor Aharonovich, ^{5,6} and Jean-Philippe Tetienne^{1,*}

¹School of Science, RMIT University, Melbourne, VIC 3001, Australia
²School of Physics, University of Melbourne, VIC 3010, Australia
³Centre for Quantum Computation and Communication Technology,
School of Physics, University of Melbourne, VIC 3010, Australia
⁴National Institutes for Quantum Science and Technology (QST),
1233 Watanuki, Takasaki, Gunma 370-1292, Japan
⁵School of Mathematical and Physical Sciences, University of Technology Sydney, Ultimo, NSW 2007, Australia
⁶ARC Centre of Excellence for Transformative Meta-Optical Systems,
University of Technology Sydney, Ultimo, NSW 2007, Australia

Detecting magnetic noise from small quantities of paramagnetic spins is a powerful capability for chemical, biochemical, and medical analysis. Quantum sensors based on optically addressable spin defects in bulk semiconductors are typically employed for such purposes, but the 3D crystal structure of the sensor inhibits the sensitivity by limiting the proximity of the defects to the target spins. Here we demonstrate the detection of paramagnetic spins using spin defects hosted in hexagonal boron nitride (hBN), a van der Waals material which can be exfoliated into the 2D regime. We first create negatively charged boron vacancy (V_B^-) defects in a powder of ultrathin hBN nanoflakes (< 10 atomic monolayers thick on average) and measure the longitudinal spin relaxation time (T_1) of this system. We then decorate the dry hBN nanopowder with paramagnetic Gd³⁺ ions and observe a clear T_1 quenching, under ambient conditions, consistent with the added magnetic noise. Finally, we demonstrate the possibility of performing spin measurements including T_1 relaxometry using solution-suspended hBN nanopowder. Our results highlight the potential and versatility of the hBN quantum sensor for a range of sensing applications, and pave the way towards the realisation of a truly 2D, ultrasensitive quantum sensor.

Optically addressable spin defects in solids have been a significant driver in the advancement of practical applications for highly sensitive quantum measurement and detection devices in a variety of fields including geoscience, materials science, and biology [1-4]. One promising capability of solid-state quantum sensors is being able to probe weak, fluctuating magnetic fields under ambient conditions and at sub-micrometer scales, which cannot typically be accessed by existing techniques such as nuclear magnetic resonance. The most prominent example of such a nanoscale sensor is the nitrogen-vacancy (NV) centre in diamond, which has been successfully employed to interrogate magnetic noise from a variety of sources, from magnons in ferromagnetic materials [5, 6] to electric current fluctuations in conductors [7, 8] to paramagnetic spins in molecular systems [9–13]. The detection of paramagnetic spins, i.e. unpaired electrons that produce a fast fluctuating magnetic noise, is especially relevant in the chemical, biological and medical sciences. For example, NV-based noise sensing has been applied to detect trace amounts of ions in aqueous solutions [14, 15], monitor the generation of free radicals in cells [16, 17], determine iron load in ferritin proteins [18], and has been proposed as the basis for new methods for rapid and sensitive virus detection [19]. In the latter proposal and similar biosensing demonstrations [19, 20], the biochemical signal of interest (e.g. the presence of a specific viral

particle or a change of pH) is transduced into magnetic noise using a paramagnetic molecule, typically a gadolinium (Gd) complex, which is attached to the surface of the quantum sensor.

The method of choice in many of these applications is measuring the longitudinal spin relaxation time (T_1) of the defect, which is sensitive to magnetic fluctuations at the defect's spin resonance frequency, ω_0 [9–13]. The change in relaxation rate induced by a nearby paramagnetic spin, $\Gamma_1^{\rm ext} = 1/T_1^{\rm ext}$, scales with the distance d between the sensor (spin defect) and the target spin as $\Gamma_1^{\rm ext} \propto d^{-6}$ [9, 10]. This strong distance dependence necessitates the defects be located close to the surface of the host crystal, in order to maximise sensitivity to spins located outside. However, spin defects in bulk 3D crystals face a practical limit, as the surface is typically plagued with dangling bonds and other sub-bandgap electronic states which compromise the charge- and photostability of near-surface defects [21–23]. For instance, an average minimum depth of at best or greater than $d \approx 5 \,\mathrm{nm}$ is typically observed for NV ensembles created near an optimised flat diamond surface [24–26]. Additionally, these unwanted surface states are often paramagnetic [22, 27] and cause a background magnetic noise obscuring the external signal of interest. These effects are especially severe in nanodiamonds with their high surface-to-volume ratio [10], limiting their practical sensitivity to external signals. Given nanodiamonds are widely used for chemical and bio-sensing applications owing to their convenience and compatibility with in-

^{*} jean-philippe.tetienne@rmit.edu.au

solution measurements [12, 16, 17, 19, 20, 28], there is a strong motivation for exploring new quantum sensing systems that may afford shorter sensor-target distances and reduced intrinsic magnetic noise while preserving the versatility of nanodiamonds.

Spin defects hosted in a layered van der Waals (vdW) material could provide a solution to both of these problems. Indeed, vdW materials can often be exfoliated into atomically thin flakes while maintaining near-perfect crystallinity and defect-free surfaces. As such, it may be possible to engineer robust spin defects that reside within just a few atomic sites from the surface (i.e. $d \approx 1-2 \,\mathrm{nm}$) and with no surface-induced background magnetic noise, which could open a new frontier in ultrasensitive quantum sensing. Recently, hexagonal boron nitride (hBN) has emerged as a promising material platform to realise such ultrathin quantum sensors [29–37]. hBN is an exfoliable, air-stable vdW material and is host to a robust, optically addressable spin defect, the negatively charged boron vacancy (V_B^-) [29, 38]. The V_B^- defect can be introduced in the hBN lattice through a variety of irradiation methods [39, 40], and several demonstrations of quantum sensing have subsequently been reported, including the detection and imaging under ambient conditions of static magnetic fields, temperature and strain [30, 33–36], and the imaging of magnetic noise from a ferromagnetic material at cryogenic temperatures [37].

In this work, we demonstrate the first detection of magnetic noise from paramagnetic spins with an hBN quantum sensor, under ambient conditions. In contrast with previous quantum sensing demonstrations which employed hBN flakes exfoliated from bulk crystals [30, 33– 36], here we use hBN nanopowder, a convenient and cost-effective alternative which enables sensing in a wider range of environments including in solution. We first characterise the spin properties of the $V_{\rm B}^-$ defects created in hBN nanopowder, and find the T_1 time is comparable to that in a bulk hBN crystal. We then dress the nanopowder with Gd³⁺ ions, a common paramagnetic contrast agent used in magnetic resonance imaging, and observe a reliable T_1 quenching effect which illustrates the ability to detect external noise sources. Finally, we perform spin measurements of the nanopowder suspended in water and again observe a T_1 reduction upon adding Gd³⁺ ions, demonstrating the possibility of in-solution sensing experiments. These results establish hBN nanopowder as a promising platform for magnetic noise sensing applications, and motivate further work to improve the sensitivity of the hBN quantum sensor, including by making hBN flakes approaching the 2D limit. This could make hBN quantum sensors a viable alternative to nanodiamonds for a range of chemical and biosensing applications such as ultrasensitive virus detection and other rapid point-of-care tests.

RESULTS AND DISCUSSION

Our quantum sensor is based on commercially available hBN nanopowder sourced from Graphene Supermarket. The powder is composed of flake-like particles with a thickness of $6 \pm 3 \,\mathrm{nm}$ (mean \pm standard deviation) as determined by atomic force microscopy measurements, and a lateral size of order 100 nm (see SI, Sec. II). The 6 nm mean thickness corresponds to ≈ 9 atomic monolayers. In principle, the size of these nanoflakes can be further reduced through liquid-phase exfoliation [41, 42], making it an ideal candidate to realise quantum sensors approaching the 2D limit (i.e. made up of a single monolayer of hBN). The as-received powder was electron irradiated to create a high density of vacancies throughout the entire material, some of which forming the desired $V_{\rm B}^$ defects [40]. The irradiated powder was used as is, in its dry form, or suspended in water or isopropanol to make powder films by drop-casting or to perform in-solution measurements.

Spin measurements with hBN nanopowder

We first characterised the dry hBN nanopowder following electron irradiation, to establish a baseline of its optical and spin properties. To this end, the powder was placed directly onto the surface of a printed circuit board (PCB) with a microwave (MW) waveguide to enable driving of the V_B^- 's electron spin transitions. A schematic of the experiment is shown in Fig. 1(a), and the crystal structure of the V_B^- defect in Fig. 1(b). Small clumps of hBN nanopowder are visible in the photograph Fig. 1(c), which were imaged using a widefield optical microscope [Fig. 1(d,e)]. The V_B^- defects are excited with a green laser ($\lambda = 532 \,\mathrm{nm}$) and the resulting photoluminescence (PL) in the near-infrared ($\lambda = 750 - 900 \,\mathrm{nm}$) imaged by a camera [Fig. 1(e)], showing uniform PL across the clump. The ground state of the $V_{\rm B}^-$ defect is a spin triplet (S=1) which is polarised into the $|0\rangle$ state upon laser excitation [Fig. 1(f)]. When left in the dark, this unequal population distribution decays back to thermal equilibrium (an equal mixture of all three spin states $|0,\pm 1\rangle$) at a rate $\Gamma_1 = 1/T_1$ [43]. In general, the total relaxation rate is the sum of intrinsic and extrinsic contributions, $\Gamma_1 = \Gamma_1^{\rm int} + \Gamma_1^{\rm ext}$, where $\Gamma_1^{\rm ext}$ may be caused e.g. by paramagnetic spins external to the hBN crystal, as we will demonstrate later. Importantly, the spin state can be read out optically owing to spin-dependent PL [29], which will allow Γ_1 to be measured. Moreover, by applying a MW field of variable frequency, an optically detected magnetic resonance (ODMR) spectrum can be obtained [Fig. 1(g)], revealing a broad resonance at $\omega_0 \approx 2\pi \times 3.45$ GHz corresponding to the electronic spin transitions $|0\rangle \rightarrow |\pm 1\rangle$. The 2% spin contrast obtained in this pulsed-ODMR spectrum is in line with previous reports on similar powders [32].

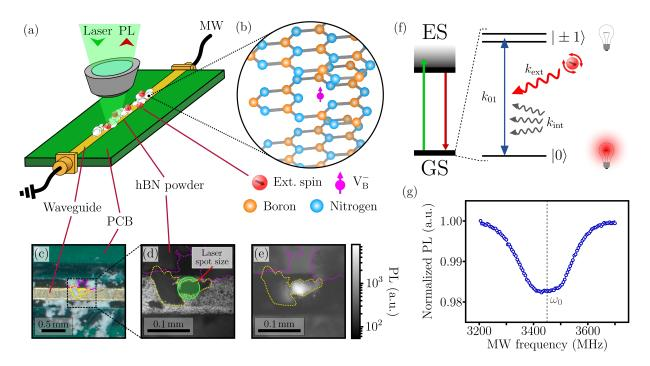


FIG. 1. Quantum sensing with hBN nanopowder. (a) Schematic representation of the experimental setup. Electronirradiated hBN nanopowder (represented as a collection of white flakes) is deposited onto a printed circuit board (PCB) with a microwave (MW) waveguide. The spin state of the V_B^- defects in the powder is optically measured via illumination with a green laser and collection of the photoluminescence (PL), which can be used to sense external paramagnetic spins (represented as red spheres) through their magnetic noise. (b) Crystal structure of the V_B^- defect in the hBN lattice. (c) True-colour photograph of hBN powder on the PCB. (d) Reflection micrograph (red channel only, displayed on a grey intensity scale) of a zoomed-in section from (c). Powder on the MW waveguide is outlined in yellow while on the PCB it is highlighted in pink. The approximate position and spot size of the laser used for PL measurements is also shown. (e) Corresponding PL image ($\lambda = 750 - 900$ nm spectral band) taken under laser illumination ($\lambda = 532$ nm) and displayed on a log scale. (f) Simplified energy level structure of the V_B^- defect. Laser illumination populates the excited state (ES) which undergoes spin-dependent PL to return to the ground state (GS). This process selectively populates the GS spin sub-level $|0\rangle$. The population imbalance then decays back to equilibrium with a two-way transition rate $k_{01} = k_{\text{int}} + k_{\text{ext}}$ which has both intrinsic (k_{int}) and external (k_{ext}) contributions. The observed relaxation rate out of $|0\rangle$ is given by $\Gamma_1 = 3k_{01}$. (g) Typical pulsed-ODMR spectrum measured for the hBN nanopowder in zero magnetic field.

Intrinsic T_1 time

To assess the viability of the hBN nanopowder for T_1 based magnetic noise sensing, we first characterised the intrinsic T_1 time of the dry powder. The measurement sequence is depicted in Fig. 2(a) and consists of laser pulses, required to initialise and read out the spin state, separated by a dark time τ during which a T_1 decay takes place. A reference measurement including a resonant MW pulse is performed to remove common-mode variations and extract the spin imbalance, which decays towards zero as τ is increased, as shown in the example decay curves in Fig. 2(b). Here, the PL data is integrated from a $15 \times 15 \,\mu\text{m}^2$ region of powder which is uniformly illuminated by the laser. We found the curves are generally well fit by a mono-exponential function, $e^{-\tau/T_1}$, from which T_1 is obtained (see further analysis details in the SI. Sec. IV).

In Fig. 2(b), two types of powder are measured and compared to a large ($\sim 100\,\mu\mathrm{m}$) flake exfoliated from a high-purity bulk hBN crystal (PL image shown as inset of

Fig. 2(b)). Powder 1 received the lowest electron irradiation dose $(2 \times 10^{18} \,\mathrm{cm}^{-2})$ and returns $T_1 = 19.5 \pm 0.8 \,\mu\mathrm{s}$ (here the uncertainty corresponds to the standard error from the fit). For powder 2, the irradiation dosage was increased by $2.5 \times$ to 5×10^{18} cm⁻² and T_1 was measured as $T_1 = 17.6 \pm 0.6 \,\mu\text{s}$. For the bulk crystal, which was electron irradiated to the same dose as powder 1, T_1 was slightly lower, $T_1 = 14.0 \pm 0.8 \,\mu\text{s}$. The small differences in T_1 may be due to different levels of crystal damage, as was suggested by Guo et al. [44]; here we speculate that the powder may experience less damage than the bulk crystal at the same nominal irradiation dose due to more efficient thermalisation during the irradiation process. Importantly, the T_1 values measured for our nanopowders, despite a mean flake thickness of only 6 nm, are comparable to the value reported by Gottschol et al. [43] for a neutron-irradiated bulk crystal ($T_1=18\,\mu\mathrm{s}$), which is the largest T_1 value reported to date for V_B^- at room temperature. Thus, nanopowders appear as an ideal platform for T_1 -based sensing, available in much higher volume and at a lower cost compared to flakes made from bulk

crystals.

We also assessed possible T_1 spatial variations across a clump of hBN powder. A T_1 map is shown in Fig. 2(c) for a typical clump, with the corresponding PL image shown in Fig. 2(d). The measured T_1 is found to be relatively uniform across the clump, with a standard deviation of about 1μ s comparable with the uncertainty from the fitting of individual pixels. On a larger scale,

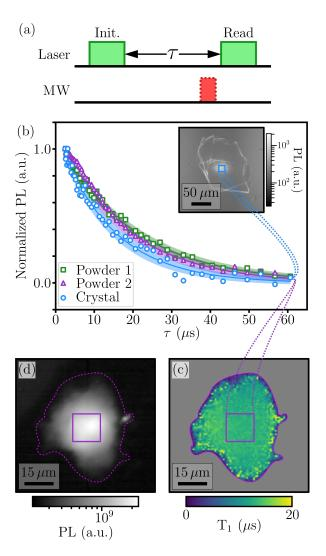


FIG. 2. T_1 relaxation in hBN nanopowder. (a) Pulse sequence for T_1 measurements. The laser acts both to initialise the spin state and read it out through the PL intensity. For each dark time τ , two PL measurements are performed, with and without the MW pulse, for normalisation purposes. (b) Spin relaxation curves for the V_B^- defects in two nanopowder samples which received different irradiation doses (powder 2 higher than powder 1, see text) and in a bulk crystal flake. Solid lines are single exponential fit; shaded areas indicate one standard error for the fit parameters. Inset: PL image of the bulk crystal flake, displayed on a log scale. (c) Spatial map of T_1 for a clump of hBN nanopowder. Area external to the clump is masked as it contains no hBN powder. (d) The corresponding PL image of the clump plotted with a log scale.

we observed slightly larger variations up to $\pm 10\%$ for the mean T_1 of distinct clumps of powder of the same type, and from different spatial locations within a continuous film of powder (as we will see in Fig. 3). Such variations may be due to local temperature variations (as laser and MW absorption leads to some amount of heating) or reflect measurement and analysis uncertainties, see Sec. IV and V of the SI for further discussions. In the following, we will study T_1 changes caused by external magnetic signals, keeping all measurement conditions constant otherwise.

Detection of external paramagnetic spins

We now test the possibility of detecting external paramagnetic spins with the hBN nanopowder, by adding a solution of gadolinium trichloride (GdCl₃). Due to the high spin of the Gd^{3+} ion $(S = \frac{7}{2})$, gadolinium complexes are commonly used as paramagnetic relaxation agents in magnetic resonance imaging. To allow for systematic measurements, we first prepare a uniform film of hBN nanopowder by suspending the powder [powder 2 from Fig. 2(b)] in isopropanol and drop-casting onto a MW waveguide [Fig. 3(a)]. A series of T_1 measurements are made at multiple random locations along the waveguide to gather a reference distribution of T_1 times, giving the top histogram in Fig. 3(b). The mean value is $T_1 = 16.3 \pm 1.3 \,\mu \text{s}$ where here the error bar corresponds to the standard deviation from the histogram. The spread is consistent with the variation of up to $\pm 10\%$ observed and discussed previously in relation to Fig. 2.

Following these reference measurements, a drop of GdCl₃ solution is deposited on the hBN film and allowed to percolate through the powder. Evaporation of the water by heating then leaves the hBN nanoflakes surrounded by a highly concentrated medium of paramagnetic Gd³⁺ ions. Example relaxation curves before and after adding Gd^{3+} are plotted in Fig. 3(c), showing a clear T_1 reduction upon adding Gd³⁺. Repeating the measurements at multiple locations [bottom histogram in Fig. 3(b)], we find that all T_1 values measured are shorter compared to the bare powder, with a mean value of $T_1 = 11.3 \pm 1.2 \,\mu\text{s}$, a 30% reduction, significantly larger than the $\lesssim 10\%$ uncertainty. This T_1 reduction corresponds to an additional relaxation rate of $\Gamma_1^{\rm ext} = 30 \pm 10 \, {\rm kHz}$. Furthermore, we performed successive T_1 measurements (one every 5 s) at a given location and found T_1 to be stable over many minutes of monitoring [Fig. 3(d)], with again a clear offset in the presence of Gd³⁺. Combined, these results indicate a robust T_1 quenching effect by the Gd^{3+} spins. Note, we repeated these experiments with higher concentrations of the GdCl₃ solution, and by applying multiple doses of the solution, and found a similar level of T_1 quenching in all cases, suggesting that the resulting density of Gd³⁺ spins around the hBN flakes has reached a saturation. On the other hand, repeating the process using pure water or a highly diluted GdCl₃ solution led to no

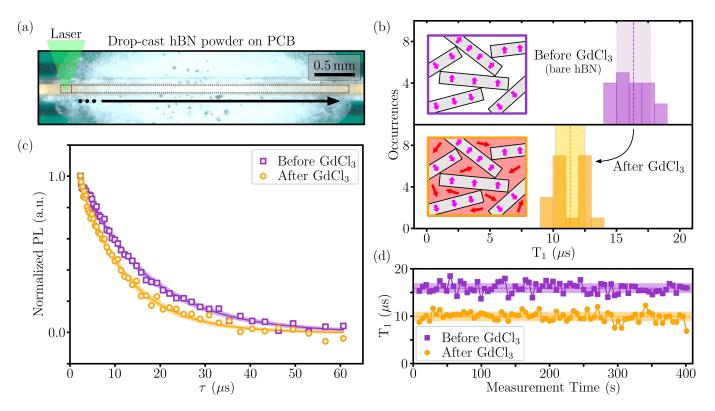


FIG. 3. Quenching T_1 with external paramagnetic spins. (a) Photograph of hBN nanopowder film formed by dropcasting. Numerous T_1 measurements are taken at random distinct locations along the direction indicated by the arrow. The drop-cast nanopowder is then dosed with a solution of GdCl₃, and the T_1 measurements repeated. (b) Histograms for 20 T_1 measurements taken before (top histogram) and after (bottom) application of the GdCl₃ solution (100 mM concentration in water). The vertical dotted lines represent the average recorded T_1 and the shaded area is one standard deviation either side of the average. (c) Representative spin relaxation curves selected from each histogram in (b). Solid lines are single exponential fit; shaded areas indicate one standard error for the fit parameters. (d) Time traces of T_1 recorded before and after application of the GdCl₃ solution. Each data point corresponds to 5 s of signal integration.

measurable change in T_1 .

To verify the observed T_1 reduction is consistent with magnetic noise from the Gd^{3+} spins, we assume each hBN nanoflake is surrounded by pure GdCl_3 and contain V_B^- defects located at a distance d from either surface of the flake of thickness 2d (see Sec. VI of the SI). The Gd^{3+} spins produce a randomly fluctuating magnetic field with a correlation time τ_c , which increases the relaxation rate of the V_B^- spins by [9, 10]

$$\Gamma_1^{\text{ext}} = 3\gamma_e^2 B_\perp^2 \frac{\tau_c}{1 + \omega_0^2 \tau_c^2},\tag{1}$$

where γ_e is the electron gyromagnetic ratio and B_{\perp}^2 is the variance in the transverse magnetic field experienced by the V_B^- spins. $\Gamma_1^{\rm ext}$ is maximised when $\tau_c = 1/\omega_0 \approx 50$ ps, which is a typical order of magnitude for ${\rm Gd}^{3+}$ complexes [9]. Assuming this maximum effect, we find the observed $\Gamma_1^{\rm ext}$ is reproduced for a flake thickness of $2d \approx 10$ nm, in good agreement with the 6 ± 3 nm thickness of our flakes. This supports our claim that the observed T_1 quenching is caused by the magnetic noise from the added ${\rm Gd}^{3+}$ spins.

Spin measurements in solution

Many applications of T_1 -based sensing involve a liquid environment, for instance detecting ions and viruses in aqueous solutions [14, 15, 19] or free radicals in cells [16, 17], or to measure the pH of a solution [20]. To test the sensing capabilities of hBN in a wet environment, we performed spin measurements of the nanopowder suspended in water. First, a drop of the hBN solution was placed on a MW waveguide and a pulsed-ODMR spectrum recorded [Fig. 4(a)]. As shown in the photographs Fig. 4(b), the solution has a white opaque appearance, such that the collected PL signal must initially come from the top-most part of the colloidal suspension. The water was found to evaporate completely after a few minutes of continuous measurement, leaving behind a dry hBN powder film [Fig. 4(c)]. Comparing the ODMR spectra taken before and after evaporation [Fig. 4(a)], we see that while the contrast remains relatively unchanged $(\approx 1\%)$, the resonance is shifted towards lower frequencies by ≈ 50 MHz upon evaporation. This decrease in ω_0 , which here corresponds to the zero-field splitting parameter of the V_B spin, implies an increase in local temper-

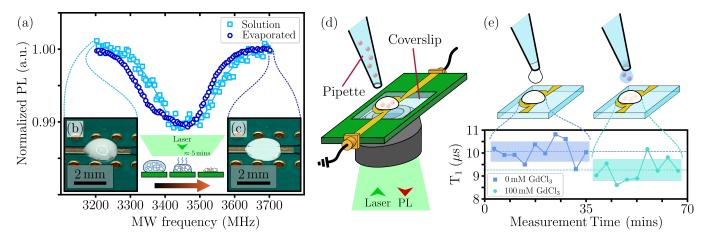


FIG. 4. Solution-based spin measurements. (a) ODMR spectra from hBN nanopowder recorded before and after evaporation of the host water. (b,c) Photographs of the hBN nanopowder on the PCB before (b) and after (c) water evaporation. In (b), the powder forms a colloidal suspension, whereas in (c) the powder forms a dry film as in Fig. 3(a). (d) Schematic of the experimental setup for in-solution T_1 sensing. The inverted geometry facilitates addition of paramagnetic ions and minimises measurement-induced heating allowing extended measurement times. (e) Time trace of T_1 measured from the suspension, with 100 mM of GdCl₃ added after 35 minutes. The horizontal dashed lines represent the average T_1 from before and after adding GdCl₃, with the shading representing one standard deviation. Note, T_1 is shorter even in pure water compared to the dry powder, which may be due to a change in the internal spin or charge environment of the hBN flakes.

ature of $\approx 70\,\mathrm{K}$ [30, 32]. The rapid evaporation followed by a dramatic temperature increase can be explained by the presence of significant heating due to local laser and MW absorption, which is initially dissipated as latent heat during the evaporation phase thus keeping the solution relatively cool, until the water has fully evaporated.

To facilitate in-situ addition of paramagnetic spins to the solution and T_1 measurements over extended periods of time, we next moved to a setup based on an inverted microscope configuration [Fig. 4(d)]. The hBN suspension is deposited on a glass coverslip which comprises an Ω-shaped MW waveguide. Because optical addressing occurs from below, the collected PL signal comes primarily from the hBN flakes that are closest to the glass-solution interface, and so it is possible to address a region located very close to the MW waveguide, thus requiring a significantly reduced MW power. To further reduce the heating induced by the measurements, we used shorter laser pulses and a lower laser peak power. As a result, we were able to perform T_1 measurements continuously for up to an hour before complete evaporation of the water, although at the cost of a reduced signal-to-noise ratio – in future, a cuvette-based setup could be employed to allow optimised, long-term measurements [45]. As a test experiment, we monitored the T_1 time of the hBN flakes initially suspended in pure water, before adding a solution of 100 mM GdCl₃ [Fig. 4(e)]. A small reduction in T_1 is observed upon addition of the GdCl₃ solution, corresponding to an added relaxation rate of $\Gamma_1^{\rm ext} = 10 \pm 10 \, {\rm kHz}$. While the observed T_1 change is close to the measurement uncertainty, these experiments demonstrate the feasibility of in-solution magnetic noise sensing with hBN nanopowder. Note, the induced quenching Γ_1^{ext} is smaller than that observed in Fig. 3,

which is expected since here the density of Gd^{3+} ions is reduced due to the presence of solvent molecules. Using higher concentrations of Gd^{3+} ions led to additional background PL which made the T_1 measurements unreliable.

Sensitivity

The key motivation for developing quantum sensors based on vdW materials is the potential for a drastically reduced minimum distance d between sensor (spin defects) and target (e.g. paramagnetic spins), compared to 3D hosts like diamond. In the present work, for our initial demonstration of external paramagnetic spin detection, we used commercially available, off-the-shelf hBN nanopowders which had a flake thickness of $6 \pm 3 \,\mathrm{nm}$, meaning the sensing defects are located at most 5 nm from the closest surface (for the thickest flakes), which is already an improvement over state-of-the-art experiments based on NV ensembles in diamond [24–26]. Furthermore, there is ample room for optimisation of the hBN sensor, in particular liquid-phase exfoliation methods should provide a straightforward way to produce even thinner hBN flakes (a few or even a single monolayer) in large quantities [41, 42]. While there has been no report of V_B^- defects in monolayer hBN to date, V_B^- defects have been successfully detected in flakes as thin as 4 nm [46] while still exhibiting ODMR, implying the defects are within 2 nm (i.e. 3 atomic layers) of the closest surface. Compared to an NV centre at d = 5 nm (typical minimum depth observed [24–26]), a V $_{\rm B}^-$ defect at d=2 nm would increase the relaxation rate $\Gamma_1^{\rm ext}$ induced by a paramagnetic spin located at the surface by

a factor $(5/2)^6 = 244$, already a dramatic improvement. Nevertheless, a potential gain in $\Gamma_1^{\rm ext}$ due to better proximity does not guarantee an improved sensitivity to external spins. In a photon-shot-noise-limited T_1 -relaxometry experiment, the signal-to-noise ratio scales as [9, 10]

$$SNR \propto \frac{\Gamma_1^{ext}}{\sqrt{\Gamma_1^{int}}} C \sqrt{I_{PL}},$$
 (2)

where $\Gamma_1^{\rm int} = 1/T_1^{\rm int}$ is the intrinsic relaxation rate in the absence of the target spin (assumed to satisfy $\Gamma_1^{\rm int} \gg$ Γ_1^{ext}), C is the relative spin contrast, and I_{PL} is the PL signal from one readout pulse. Currently, the $V_{\rm B}^-$ defect exhibits an inferior contrast and PL output compared to the NV centre, and so will need to be improved through material optimisation or photonics engineering to enhance collection [31, 46, 47]. On the other hand, the intrinsic relaxation time observed in this work for V_B^- in hBN nanopowders $(T_1^{\rm int} \approx 15 - 20 \,\mu s)$ is similar to that of NVs in nanodiamonds of comparable size [10], which do not reach the longer relaxation times exhibited by NVs in bulk diamond but nevertheless have found widespread interest. Considering all these factors together, hBN nanopowders emerge as a viable alternative to nanodiamonds for T_1 relaxometry with the potential for an improved sensitivity to external paramagnetic spins and a lower production cost, making it appealing for applications such as high-sensitivity point-of-care diagnostics [19, 28].

CONCLUSIONS

In this work, we demonstrated the first detection of magnetic noise from paramagnetic spins under ambient conditions using a van der Waals quantum sensor, namely using optically addressable spin defects ($V_{\rm B}^-$ defects) in hBN nanopowders. We first characterised the intrinsic

spin relaxation time (T_1) of the V_B^- defects in nanopowders, which was found to be comparable to that in bulk hBN crystals. We then observed a reduction in T_1 upon the addition of paramagnetic Gd³⁺ ions, in dry conditions, demonstrating the ability to detect external noise sources. Finally, we performed spin measurements using the hBN nanopowder suspended in water, demonstrating the feasibility of in-solution sensing experiments. The sensitivity of the hBN quantum sensor for the detection of paramagnetic spins was discussed, and with further improvements (in particular, approaching the 2D limit for the host hBN flakes) could be competitive with established quantum sensing platforms such the NV centre in diamond. Our results thus suggest hBN nanopowders could be a viable and potentially more convenient and cost-effective alternative to diamond-based sensors, making it appealing for a range of chemical and biosensing applications such as ultrasensitive virus detection and other rapid point-of-care tests.

ACKNOWLEDGMENTS

This work was supported by the Australian Research Council (ARC) through grants CE170100012, CE200100010, FT200100073, DE200100279 FT220100053, and by the Office of Naval Research Global (N62909-22-1-2028). We thank Yongliang Chen for providing AFM data. The work was performed in part at the RMIT Micro Nano Research Facility (MNRF) in the Victorian Node of the Australian National Fabrication Facility (ANFF) and the RMIT Microscopy and Microanalysis Facility (RMMF). I.O.R. and A.J.H. are supported by an Australian Government Research Training Program Scholarship. S.C.S gratefully acknowledges the support of an Ernst and Grace Matthaei scholarship. P.R. acknowledges support through an RMIT University Vice-Chancellor's Research Fellowship. Part of this study was supported by QST President's Strategic Grant "QST International Research Initiative".

^[1] C. L. Degen, F. Reinhard, and P. Cappellaro, Quantum sensing, Reviews of Modern Physics 89, 035002 (2017).

^[2] R. Schirhagl, K. Chang, M. Loretz, and C. L. Degen, Nitrogen-Vacancy Centers in Diamond: Nanoscale Sensors for Physics and Biology, Annual Review of Physical Chemistry 65, 83 (2014).

^[3] L. Rondin, J.-P. Tetienne, T. Hingant, J.-F. Roch, P. Maletinsky, and V. Jacques, Magnetometry with nitrogen-vacancy defects in diamond, Reports on Progress in Physics 77, 056503 (2014).

^[4] F. Casola, T. van der Sar, and A. Yacoby, Probing condensed matter physics with magnetometry based on nitrogen-vacancy centres in diamond, Nature Reviews Materials 3, 17088 (2018).

^[5] C. Du, T. van der Sar, T. X. Zhou, P. Upadhyaya, F. Casola, H. Zhang, M. C. Onbasli, C. A. Ross, R. L.

Walsworth, Y. Tserkovnyak, and A. Yacoby, Control and local measurement of the spin chemical potential in a magnetic insulator, Science **357**, 195 (2017).

^[6] B. A. McCullian, A. M. Thabt, B. A. Gray, A. L. Melendez, M. S. Wolf, V. L. Safonov, D. V. Pelekhov, V. P. Bhallamudi, M. R. Page, and P. C. Hammel, Broadband multi-magnon relaxometry using a quantum spin sensor for high frequency ferromagnetic dynamics sensing, Nat Communications 11, 5229 (2020).

^[7] S. Kolkowitz, A. Safira, A. A. High, R. C. Devlin, S. Choi, Q. P. Unterreithmeier, D. Patterson, A. S. Zibrov, V. E. Manucharyan, H. Park, and M. D. Lukin, Probing Johnson noise and ballistic transport in normal metals with a single-spin qubit, Science 347, 1129 (2015).

^[8] A. Ariyaratne, D. Bluvstein, B. A. Myers, and A. C. B. Jayich, Nanoscale electrical conductivity imaging using a

- nitrogen-vacancy center in diamond, Nature Communications 9, 2406 (2018).
- [9] S. Steinert, F. Ziem, L. T. Hall, A. Zappe, M. Schweikert, N. Götz, A. Aird, G. Balasubramanian, L. Hollenberg, and J. Wrachtrup, Magnetic spin imaging under ambient conditions with sub-cellular resolution, Nature Communications 4, 1607 (2013).
- [10] J.-P. Tetienne, T. Hingant, L. Rondin, A. Cavaillès, L. Mayer, G. Dantelle, T. Gacoin, J. Wrachtrup, J.-F. Roch, and V. Jacques, Spin relaxometry of single nitrogen-vacancy defects in diamond nanocrystals for magnetic noise sensing, Physical Review B 87, 235436 (2013).
- [11] A. Ermakova, G. Pramanik, J. M. Cai, G. Algara-Siller, U. Kaiser, T. Weil, Y. K. Tzeng, H. C. Chang, L. P. McGuinness, M. B. Plenio, B. Naydenov, and F. Jelezko, Detection of a few metallo-protein molecules using color centers in nanodiamonds, Nano Letters 13, 3305 (2013).
- [12] S. Kaufmanna, D. A. Simpson, L. T. Hall, V. Perunicic, P. Senn, S. Steinert, L. P. McGuinness, B. C. Johnson, T. Ohshima, F. Caruso, J. Wrachtrup, R. E. Scholten, P. Mulvaney, and L. Hollenberg, Detection of atomic spin labels in a lipid bilayer using a single-spin nanodiamond probe, Proceedings of the National Academy of Sciences of the United States of America 110, 10894 (2013).
- [13] A. O. Sushkov, N. Chisholm, I. Lovchinsky, M. Kubo, P. K. Lo, S. D. Bennett, D. Hunger, A. Akimov, R. L. Walsworth, H. Park, and M. D. Lukin, All-optical sensing of a single-molecule electron spin, Nano Letters 14, 6443 (2014).
- [14] F. C. Ziem, N. S. Götz, A. Zappe, S. Steinert, and J. Wrachtrup, Highly Sensitive Detection of Physiological Spins in a Microfluidic Device, Nano Letters 13, 4093 (2013).
- [15] D. A. Simpson, R. G. Ryan, L. T. Hall, E. Panchenko, S. C. Drew, S. Petrou, P. S. Donnelly, P. Mulvaney, and L. C. L. Hollenberg, Electron paramagnetic resonance microscopy using spins in diamond under ambient conditions, Nature Communications 8, 458 (2017).
- [16] R. Sharmin, A. C. Nusantara, L. Nie, K. Wu, A. Elias Llumbet, W. Woudstra, A. Mzyk, and R. Schirhagl, Intracellular Quantum Sensing of Free-Radical Generation Induced by Acetaminophen (APAP) in the Cytosol, in Mitochondria and the Nucleus of Macrophages, ACS Sensors 7, 3326 (2022).
- [17] L. Nie, A. C. Nusantara, V. G. Damle, M. V. Baranov, M. Chipaux, C. Reyes-San-Martin, T. Hamoh, C. P. Epperla, M. Guricova, P. Cigler, G. van den Bogaart, and R. Schirhagl, Quantum sensing of free radicals in primary human dendritic cells, Nano Letters 22, 1818 (2022).
- [18] E. S. Grant, L. T. Hall, L. C. L. Hollenberg, G. McColl, and D. A. Simpson, Nonmonotonic superparamagnetic behavior of the ferritin iron core revealed via quantum spin relaxometry, ACS Nano 17, 372 (2023).
- [19] C. Li, R. Soleyman, M. Kohandel, and P. Cappellaro, SARS-CoV-2 Quantum Sensor Based on Nitrogen-Vacancy Centers in Diamond, Nano Letters 22, 43 (2022).
- [20] T. Rendler, J. Neburkova, O. Zemek, J. Kotek, A. Zappe, Z. Chu, P. Cigler, and J. Wrachtrup, Optical imaging of localized chemical events using programmable diamond quantum nanosensors, Nature Communications 8, 14701 (2017).

- [21] M. Kaviani, P. Deak, B. Aradi, T. Frauenheim, J. P. Chou, and A. Gali, Proper surface termination for luminescent near-surface nv centers in diamond, Nano Letters 14, 4772 (2014).
- [22] A. Stacey, N. Dontschuk, J. Chou, D. A. Broadway, A. K. Schenk, M. J. Sear, J. Tetienne, A. Hoffman, S. Prawer, C. I. Pakes, A. Tadich, N. P. de Leon, A. Gali, and L. C. L. Hollenberg, Evidence for primal sp2 defects at the diamond surface: Candidates for electron trapping and noise sources, Advanced Materials Interfaces 6, 1801449 (2018).
- [23] D. Bluvstein, Z. Zhang, and A. C. B. Jayich, Identifying and mitigating charge instabilities in shallow diamond nitrogen-vacancy centers, Phys Rev Lett 122, 076101 (2019).
- [24] F. Ziem, M. Garsi, H. Fedder, and J. Wrachtrup, Quantitative nanoscale MRI with a wide field of view, Scientific Reports 9, 12166 (2019).
- [25] A. J. Healey, L. T. Hall, G. A. White, T. Teraji, M. A. Sani, F. Separovic, J. P. Tetienne, and L. C. Hollenberg, Polarization Transfer to External Nuclear Spins Using Ensembles of Nitrogen-Vacancy Centers, Physical Review Applied 15, 054052 (2021).
- [26] K. S. Liu, A. Henning, M. W. Heindl, R. D. Allert, J. D. Bartl, I. D. Sharp, R. Rizzato, and D. B. Bucher, Surface nmr using quantum sensors in diamond, Proc. Natl. Acad. Sci. U.S.A. 119, e2111607119 (2022).
- [27] S. Sangtawesin, B. L. Dwyer, S. Srinivasan, J. J. Allred, L. V. H. Rodgers, K. De Greve, A. Stacey, N. Dontschuk, K. M. O'Donnell, D. Hu, D. A. Evans, C. Jaye, D. A. Fischer, M. L. Markham, D. J. Twitchen, H. Park, M. D. Lukin, and N. P. de Leon, Origins of diamond surface noise probed by correlating single-spin measurements with surface spectroscopy, Phys. Rev. X 9, 031052 (2019).
- [28] B. S. Miller, L. Bezinge, H. D. Gliddon, D. Huang, G. Dold, E. R. Gray, J. Heaney, P. J. Dobson, E. Nastouli, J. J. L. Morton, and R. A. McKendry, Spinenhanced nanodiamond biosensing for ultrasensitive diagnostics, Nature 587, 588 (2020).
- [29] A. Gottscholl, M. Kianinia, V. Soltamov, S. Orlinskii, G. Mamin, C. Bradac, C. Kasper, K. Krambrock, A. Sperlich, M. Toth, I. Aharonovich, and V. Dyakonov, Initialization and read-out of intrinsic spin defects in a van der Waals crystal at room temperature, Nature Materials 19, 540 (2020).
- [30] A. Gottscholl, M. Diez, V. Soltamov, C. Kasper, D. Krausse, A. Sperlich, M. Kianinia, C. Bradac, I. Aharonovich, and V. Dyakonov, Spin defects in hbn as promising temperature, pressure and magnetic field quantum sensors, Nature Communications 12, 4480 (2021).
- [31] X. Gao, B. Jiang, A. E. Llacsahuanga Allcca, K. Shen, M. A. Sadi, A. B. Solanki, P. Ju, Z. Xu, P. Upadhyaya, Y. P. Chen, S. A. Bhave, and T. Li, High-contrast plasmonic-enhanced shallow spin defects in hexagonal boron nitride for quantum sensing, Nano Letters 21, 7708 (2021).
- [32] W. Liu, Z.-P. Li, Y.-Z. Yang, S. Yu, Y. Meng, Z.-A. Wang, Z.-C. Li, N.-J. Guo, F.-F. Yan, Q. Li, J.-F. Wang, J.-S. Xu, Y.-T. Wang, J.-S. Tang, C.-F. Li, and G.-C. Guo, Temperature-dependent energy-level shifts of spin defects in hexagonal boron nitride, ACS Photonics 8, 1889 (2021).

- [33] A. J. Healey, S. C. Scholten, T. Yang, J. A. Scott, G. J. Abrahams, I. O. Robertson, X. F. Hou, Y. F. Guo, S. Rahman, Y. Lu, M. Kianinia, I. Aharonovich, and J.-P. Tetienne, Quantum microscopy with van der Waals heterostructures, Nature Physics 19, 87 (2023).
- [34] P. Kumar, F. Fabre, A. Durand, T. Clua-Provost, J. Li, J. Edgar, N. Rougemaille, J. Coraux, X. Marie, P. Renucci, C. Robert, I. Robert-Philip, B. Gil, G. Cassabois, A. Finco, and V. Jacques, Magnetic imaging with spin defects in hexagonal boron nitride, Phys. Rev. Appl. 18, L061002 (2022).
- [35] X. Lyu, Q. Tan, L. Wu, C. Zhang, Z. Zhang, Z. Mu, J. Zúñiga-Pérez, H. Cai, and W. Gao, Strain quantum sensing with spin defects in hexagonal boron nitride, Nano Letters 22, 6553 (2022).
- [36] T. Yang, N. Mendelson, C. Li, A. Gottscholl, J. Scott, M. Kianinia, V. Dyakonov, M. Toth, and I. Aharonovich, Spin defects in hexagonal boron nitride for strain sensing on nanopillar arrays, Nanoscale 14, 5239 (2022).
- [37] M. Huang, J. Zhou, D. Chen, H. Lu, N. J. McLaughlin, S. Li, M. Alghamdi, D. Djugba, J. Shi, H. Wang, and C. R. Du, Wide field imaging of van der Waals ferromagnet Fe3GeTe2 by spin defects in hexagonal boron nitride, Nature Communications 13, 5369 (2022).
- [38] W. Liu, N.-J. Guo, S. Yu, Y. Meng, Z.-P. Li, Y.-Z. Yang, Z.-A. Wang, X.-D. Zeng, L.-K. Xie, Q. Li, J.-F. Wang, J.-S. Xu, Y.-T. Wang, J.-S. Tang, C.-F. Li, and G.-C. Guo, Spin-active defects in hexagonal boron nitride, Materials for Quantum Technology 2, 032002 (2022).
- [39] M. Kianinia, S. White, J. E. Fröch, C. Bradac, and I. Aharonovich, Generation of spin defects in hexagonal boron nitride, ACS Photonics 7, 2147 (2020).
- [40] F. F. Murzakhanov, B. V. Yavkin, G. V. Mamin, S. B. Orlinskii, I. E. Mumdzhi, I. N. Gracheva, B. F. Gabbasov, A. N. Smirnov, V. Y. Davydov, and V. A. Soltamov, Creation of negatively charged boron vacancies in hexagonal boron nitride crystal by electron irradiation and mechanism of inhomogeneous broadening of boron vacancy-related spin resonance lines, Nanomaterials (Basel) 11, 1373 (2021).
- [41] K. Zhang, Y. Feng, F. Wang, Z. Yang, and J. Wang, Two dimensional hexagonal boron nitride (2d-hbn): synthesis, properties and applications, J. Mater. Chem. C 5, 11992 (2017).
- [42] Y. Chen, M. T. Westerhausen, C. Li, S. White, C. Bradac, A. Bendavid, M. Toth, I. Aharonovich, and T. T. Tran, Solvent-exfoliated hexagonal boron nitride nanoflakes for quantum emitters, ACS Applied Nano Materials 4, 10449 (2021).
- [43] A. Gottscholl, M. Diez, V. Soltamov, C. Kasper, A. Sperlich, M. Kianinia, C. Bradac, I. Aharonovich, and V. Dyakonov, Room temperature coherent control of spin defects in hexagonal boron nitride, Science Advances 7, eabf3630 (2021).
- [44] N.-J. Guo, W. Liu, Z.-P. Li, Y.-Z. Yang, S. Yu, Y. Meng, Z.-A. Wang, X.-D. Zeng, F.-F. Yan, Q. Li, J.-F. Wang, J.-S. Xu, Y.-T. Wang, J.-S. Tang, C.-F. Li, and G.-C. Guo, Generation of Spin Defects by Ion Implantation in Hexagonal Boron Nitride, ACS Omega 7, 1733 (2022).
- [45] E. S. Grant, M. B. A. Olia, E. P. Walsh, L. T. Hall, G. McColl, and D. A. Simpson, Method for in-solution, high-throughput t1 relaxometry using fluorescent nanodiamonds, Preprint, arXiv.2211.14959 (2022).

- [46] X. Xu, A. B. Solanki, D. Sychev, X. Gao, S. Peana, A. S. Baburin, K. Pagadala, Z. O. Martin, S. N. Chowdhury, Y. P. Chen, T. Taniguchi, K. Watanabe, I. A. Rodionov, A. V. Kildishev, T. Li, P. Upadhyaya, A. Boltasseva, and V. M. Shalaev, Greatly enhanced emission from spin defects in hexagonal boron nitride enabled by a low-loss plasmonic nanocavity, Nano Letters 23, 25 (2023).
- [47] J. E. Froch, L. P. Spencer, M. Kianinia, D. D. Totonjian, M. Nguyen, A. Gottscholl, V. Dyakonov, M. Toth, S. Kim, and I. Aharonovich, Coupling spin defects in hexagonal boron nitride to monolithic bullseye cavities, Nano Letters 21, 6549 (2021).
- [48] B. A. Myers, A. Ariyaratne, and A. C. B. Jayich, Double-quantum spin-relaxation limits to coherence of near-surface nitrogen-vacancy centers, Phys Rev Lett 118, 197201 (2017).
- [49] A. Gardill, M. Cambria, and S. Kolkowitz, Fast Relaxation on Qutrit Transitions of Nitrogen-Vacancy Centers in Nanodiamonds, Physical Review Applied 13, 034010 (2020).
- [50] T. Rosskopf, A. Dussaux, K. Ohashi, M. Loretz, R. Schirhagl, H. Watanabe, S. Shikata, K. M. Itoh, and C. L. Degen, Investigation of surface magnetic noise by shallow spins in diamond, Phys Rev Lett 112, 147602 (2014).
- [51] I. C. Barbosa, J. Gutsche, and A. Widera, Impact of charge conversion on nv-center relaxometry, Preprint, arXiv.2301.01063 (2023).
- [52] S. E. Lillie, D. A. Broadway, N. Dontschuk, S. C. Scholten, B. C. Johnson, S. Wolf, S. Rachel, L. C. L. Hollenberg, and J.-P. Tetienne, Laser Modulation of Superconductivity in a Cryogenic Wide-field Nitrogen-Vacancy Microscope, Nano Letters 20, 1855 (2020).

Supplementary Information for the manuscript "Detection of paramagnetic spins with an ultrathin van der Waals quantum sensor"

I. EXPERIMENTAL SETUP

The optical and spin measurements reported in the main text were carried out on a custom-built wide-field fluorescence microscope. Optical excitation from a continuous-wave (CW) $\lambda=532$ nm laser (Laser Quantum Opus 2 W) was gated using an acousto-optic modulator (Gooch & Housego R35085-5) and focused using a widefield lens (f=400 mm) to the back apearture of the objective lens (Nikon S Plan Fluor ELWD 20x, NA = 0.45). The photoluminescence (PL) from the $V_{\rm B}^-$ defects is separated from the excitation light with a dichroic mirror and filtered using a 750 nm longpass filter before being imaged using a tube lens (f=300 mm) onto a scientific CMOS camera (Andor Zyla 5.5-W USB3). In all experiments except Fig. 4(d,e) of the main text, the laser spot diameter ($1/e^2$) at the sample was about 50 μ m and the total CW laser power 500 mW, which gives a maximum intensity of about $0.5 \, {\rm mW}/\mu {\rm m}^2$ in the centre of the spot. In Fig. 4(d,e), the laser power was reduced to 200 mW.

Microwave (MW) excitation was provided by a signal generator (Windfreak SynthNV PRO) gated using an IQ modulator (Texas Instruments TRF37T05EVM) and amplified (Mini-Circuits HPA-50W-63+). A pulse pattern generator (SpinCore PulseBlasterESR-PRO 500 MHz) was used to gate the excitation laser and MW and to synchronise the image acquisition. The output of the amplifier was connected to the printed circuit board (PCB) which was terminated by a $50\,\Omega$ termination. In all experiments except Fig. 4(d,e) of the main text, MW driving was achieved via a coplanar waveguide built in the PCB, with the hBN powder deposited directly onto the surface of the waveguide. In Fig. 4(d,e), the MW was delivered by an Ω -shaped resonator fabricated onto a glass coverslip mounted on a PCB, with the hBN suspension deposited on the coverslip. All measurements were performed at room temperature in ambient atmosphere.

II. SAMPLE PREPARATION

All experiments performed in this work [except the bulk crystal measurement in Fig. 2(b)] used hBN nanopowder sourced from Graphene Supermarket (BN Ultrafine Powder). As the as-received powder contained no measurable concentration of V_B^- defects, we subjected the powder to electron irradiation with a beam energy of 2 MeV. The irradiation dose was 2×10^{18} cm⁻² (called 'powder 1' in the main text) or 5×10^{18} cm⁻² ('powder 2'). PL spectra of the different powders under $\lambda = 532$ nm excitation [Fig. S1] show the appearance of the characteristic V_B^- emission upon irradiation, i.e. a broad peak centred around 800 nm wavelength [29].

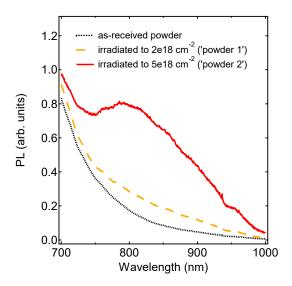


FIG. S1. PL spectra of the hBN nanopowder following different electron irradiation conditions: no irradiation (as received), 2×10^{18} cm⁻² dose ('powder 1'), and 5×10^{18} cm⁻² ('powder 2'). These spectra were obtained with the same setup as described in Sec. I, with 500 mW of laser power over a 50 μ m spot, except that the PL emission was passed through a 550 nm longpass filter to block the laser light and sent to a spectrometer (Ocean Insight Maya2000-Pro).

For the experiments in Fig. 1 and 2 of the main text, the irradiated powder was transferred to the PCB with the tip of a pair of tweezers, forming large clumps (10's of μ m in size). For the experiments in Fig. 3 of the main text, the irradiated powder was suspended in isopropyl alcohol (IPA) at a concentration of 20 mg/mL and sonicated for 30 min using a horn-sonicator. The sediment from the suspension was drawn using a pipette, then drop cast on the PCB, forming a relatively continuous film. For the experiments in Fig. 4 of the main text, the powder was suspended in water (20 mg/mL) and a drop of the suspension was deposited on the PCB [Fig. 4(a-c)] or on the coverslip [Fig. 4(d,e)].

To characterise the size of the hBN nanoflakes, we performed atomic force microscope (AFM) measurements of powder 2. The particle stock suspension (20 mg/mL in IPA) was diluted to a concentration of 1 mg/mL, sonicated for 10 min in a sonication bath, centrifuged at 1000 rcf for 1 min to remove large aggregates, and the supernatant was spin coated at 2000 rpm onto a clean silicon wafer. AFM images were acquired using an Oxford Instruments Asylum Research MFP-3D Infinity AFM in AC mode using a Budget Sensors Tap300AL-G probe. The images were collected at a scan rate of 1 Hz. A typical AFM image is shown in Fig. S2(a), where isolated flakes are visibe. The images were analysed to extract the average thickness of each individual flake, excluding all large particle aggregates, giving the histogram Fig. S2(b). The flake thickness ranges mainly between 2 nm and 9 nm, with a mean value of 6 nm and a standard deviation of 3 nm. The lateral size of the flakes is of the order of 100 nm. These values are consistent with previous measurements of powder from the same manufacturer [42]. They are also consistent with the specific surface area of $\sim 20 \, \mathrm{m}^2/\mathrm{g}$ measured by the manufacturer.

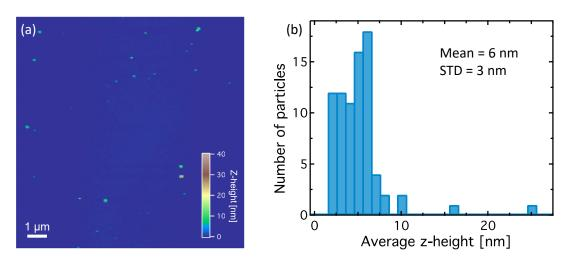


FIG. S2. (a) Typical AFM image of hBN nanoflakes spin-coated onto a silicon wafer. (b) Histogram of the average hBN particle height.

For the T_1 quenching experiments reported in Fig. 3 and 4 of the main text, a solution of GdCl₃ was first prepared by dissolving GdCl₃ solid powder (Sigma-Aldrich, 99.99% purity) in water to a concentration of 100 mM. A drop of the solution was then deposited on the hBN film. The PCB was then heated immediately to 80°C for 5 min to evaporate any remaining water. We note that the density of the hBN nanopowder in dry form is $0.30 \,\mathrm{g/cm^3}$ according to the manufacturer, which is 7 times less than the density of bulk hBN ($2.1 \,\mathrm{g/cm^3}$). This indicates that the dry powder forms a largely porous medium. We conjecture that the GdCl₃ solution percolates through the hBN film in such a way that most individual hBN flakes are completely surrounded by GdCl₃ upon solvent evaporation, as depicted in the inset of Fig. 3(b).

Finally, the bulk crystal measurement in Fig. 2(b) was done using a high-purity crystal purchased from HQ Graphene. The crystal was electron irradiated to a dose of $2 \times 10^{18} \, \mathrm{cm}^{-2}$ with a beam energy of 2 MeV. Following irradiation, a $\sim 1 \, \mu$ m-thick flake was exfoliated using scotch tape and transferred to a quartz coverslip placed on a PCB with a MW waveguide. To avoid possible edge effects, the T_1 time was measured near the centre of the flake where the PL from the $V_{\rm B}$ defects was uniform.

III. DATA ACQUISITION

The spin measurements reported in the main text were obtained using the wide-field setup described in Sec I. For optically detected magnetic resonance (ODMR) spectra, the pulse sequence was typically: $0.5 \,\mu s$ laser pulse, $0.5 \,\mu s$ wait time, $30 \, ns$ MW pulse (corresponding to a π spin flip as estimated from a Rabi measurement). This sequence was

repeated thousands of times to fill the exposure time of the camera, generally set to 10 ms. The MW frequency was swept such that one camera frame is recorded for each MW frequency value, with a reference frame with the MW off recorded every other frame to remove common-mode noise – forming a normalised ODMR spectrum (PL with MW on divided by PL with MW off) such as that shown in Fig. 1(g). The MW sweep was repeated tens to hundreds of times to improve the signal-to-noise ratio (SNR), corresponding to several minutes of acquisition per spectrum.

 T_1 measurements were obtained by applying a series of laser pulses separated by a variable dark time τ . For each τ value, the base pulse sequence (laser pulse, wait time τ , optional MW pulse) was repeated $N = t_{\rm cam}/t_0$ times where t_0 is the duration of the base sequence with the shortest τ , and $t_{\rm cam} = 10\,{\rm ms}$ is the minimum camera exposure time. As τ is increased, we keep N fixed and increase the camera exposure time accordingly. For each τ value, a camera frame is acquired without the MW pulse ('signal'), followed by a camera frame with the MW pulse ('reference'). Example PL traces $S(\tau)$ and $R(\tau)$ thus obtained (without and with the MW pulse, respectively), are shown in Fig. S3(a). The reference trace serves to remove common-mode variations and normalise the data, as will be discussed in Sec. IV B. The entire τ sweep is repeated over several minutes to improve the SNR in the same way we do for ODMR measurements.

The laser pulse acts as both initialisation and readout of the V_B^- spin state. Its duration (between $0.5\,\mu s$ and $4\,\mu s$ in our experiments) is chosen long enough to initialise the spin in the $|0\rangle$ state with sufficient fidelity as appropriate for T_1 measurements while preserving a good spin contrast, as will be discussed in Sec. IV C. The MW pulse was around 30 ns long typically, corresponding to a π spin flip as estimated from a Rabi measurement. The dark time τ was defined as the time between consecutive laser pulses, inclusive of the MW pulse time when present. The timing of the MW pulse was adjusted to account for the delay incurred by the AOM, such that the MW pulse occurred immediately prior to the laser pulse. For all T_1 measurements presented in the paper, $51\,\tau$ points are collected between $2\,\mu s$ to $60\,\mu s$ with exponentially weighted spacing, where we excluded the $\tau=0-2\,\mu s$ range to allow the system to fully relax to its electronic ground state.

Except in Fig. 2(c) where the T_1 data was analysed pixel by pixel to form a spatial map of T_1 , all ODMR and T_1 measurements reported integrated the data over a $15 \times 15 \,\mu\text{m}^2$ area where the laser intensity was approximately uniform.

IV. ANALYSIS OF T_1 MEASUREMENTS

A. Population dynamics in the dark

In order to analyse the T_1 measurements, we consider a simple three-level system corresponding to the three spin states $|0,\pm 1\rangle$ of the spin-1 system [see main text Fig. 1(f)]. In the dark (no laser), $|0\rangle$ and $|\pm 1\rangle$ are coupled by a two-way transition rate $k_{01} = k_{\rm int} + k_{\rm ext}$ which captures both intrinsic $(k_{\rm int})$ and external $(k_{\rm ext})$ contributions [7, 10]. For simplicity we assume that there is no coupling between $|+1\rangle$ and $|-1\rangle$, which is valid if the relaxation dynamics is dominated by magnetic effects rather than electric or phonon processes [7, 48, 49]. In Ref. [43], a strong temperature dependence of T_1 was observed for the V_B^- defect indicating a thermally activated process, but the exact mechanism remains unclear – one possibility is that T_1 relaxation is primarily due to magnetic noise from the electron spin bath with a temperature-dependent correlation time [50].

To determine the population dynamics in the dark, we solve the matrix rate equation $\partial_t \rho = \Phi \rho$ where Φ is the transition rate matrix and ρ is the population density matrix with elements $\rho_0(t)$, $\rho_{+1}(t)$, and $\rho_{-1}(t)$, which describe the time-dependent populations of the individual states in the spin-1 system. Under the above-mentioned assumption, the transition rate matrix is,

$$\Phi = \begin{bmatrix}
-k_{01} & k_{01} & 0 \\
k_{01} & -2k_{01} & k_{01} \\
0 & k_{01} & -k_{01}
\end{bmatrix}.$$
(S1)

Solving the matrix rate equation with initial populations $\rho_0(0)$, $\rho_{+1}(0)$, and $\rho_0(0)$, gives

$$\rho_0(t) = \frac{1}{3} + \left[\rho_0(0) - \frac{1}{3}\right] e^{-3k_{01}t} \tag{S2}$$

$$\rho_{\pm 1}(t) = \frac{1}{3} - \frac{1}{2} \left[\rho_0(0) - \frac{1}{3} \right] e^{-3k_{01}t} \pm \frac{1}{2} \left[\rho_{+1}(0) - \rho_{-1}(0) \right] e^{-k_{01}t} . \tag{S3}$$

By convention, T_1 is defined as the characteristic decay time out of the $|0\rangle$ state, i.e. the decay in the population of $\rho_0(t)$; thus, $\frac{1}{T_1} = 3k_{01}$.

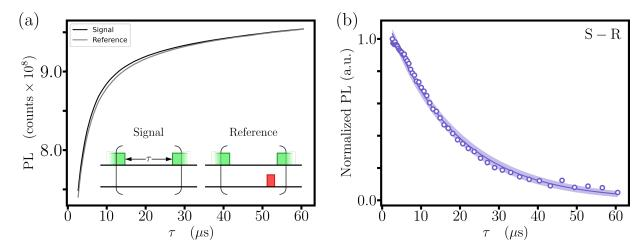


FIG. S3. (a) Typical raw traces $S(\tau)$ and $R(\tau)$ (called signal and reference, respectively) obtained from a T_1 measurement. The inset shows the pulse sequence in each case, where the reference measurement includes a MW π pulse prior to the laser readout pulse. (b) Normalised relaxation curve deduced from the raw traces in (a) using Eq. S9. The solid line is a mono-exponential fit used to extract a value for T_1 .

B. PL normalisation

Experimentally, T_1 is estimated via the PL emitted by the V_B^- defects following a dark time τ , as the PL depends on the spin state owing to an intersystem crossing [29]. One can write the PL intensity measured in a T_1 experiment as the sum

$$I(\tau) = I_{\rm B}(\tau) + A_0(\tau)\rho_0(\tau) + A_1(\tau)[\rho_{-1}(\tau) + \rho_{+1}(\tau)]$$
(S4)

where $I_{\rm B}$ is the background (spin-independent) PL, and A_0 and A_1 are the PL rates associated with the $|0\rangle$ and $|\pm 1\rangle$ states, respectively. In Eq. S4, we included a τ dependence in all the constants to highlight the importance of the choice of normalisation method [23, 51], discussed below.

As described in Sec. III, the experimental data set comprises a 'signal' trace $S(\tau)$ and a 'reference' trace $R(\tau)$, corresponding to the PL measured without and with a MW π pulse following the dark time τ , respectively. To obtain equations for $S(\tau)$ and $R(\tau)$, we substitute in the expressions for the population densities with corresponding initial populations which assume the laser perfectly initialises the $|0\rangle$ state and the MW pulse perfectly swaps the $|0\rangle$ and $|\pm 1\rangle$ populations:

$$S(\tau) = I_{\rm B}(\tau) + \left(\frac{A_0(\tau) + 2A_1(\tau)}{3}\right) \left[1 + 2\left(\frac{A_0(\tau) - A_1(\tau)}{A_0(\tau) + 2A_1(\tau)}\right)e^{-\frac{\tau}{T_1}}\right]$$
(S5)

$$R(\tau) = I_{\rm B}(\tau) + \left(\frac{A_0(\tau) + 2A_1(\tau)}{3}\right) \left[1 - \left(\frac{A_0(\tau) - A_1(\tau)}{A_0(\tau) + 2A_1(\tau)}\right) e^{-\frac{\tau}{T_1}}\right]$$
(S6)

To simplify and generalise we rewrite in terms of the spin-related PL $I_S = [A_0 + 2A_1]/3$ and the contrast $C_1 = -2C_2 = 2[A_0 - A_1]/[A_0 + 2A_1]$:

$$S(\tau) = I_{\rm B}(\tau) + I_{\rm S}(\tau) \left[1 + C_1(\tau)e^{-\frac{\tau}{T_1}} \right]$$
 (S7)

$$R(\tau) = I_{\rm B}(\tau) + I_{\rm S}(\tau) \left[1 + \mathcal{C}_2(\tau) e^{-\frac{\tau}{T_1}} \right]$$
 (S8)

Two relevant cases allow T_1 to be extracted exactly [23]. First, if the product $I_S C_1 = 2[A_0 - A_1]/3$ is constant (i.e. independent of τ), then subtraction of $R(\tau)$ from $S(\tau)$ gives a simple exponential decay

$$\mathcal{N}(\tau) := S(\tau) - R(\tau) = I_{\mathcal{S}} \mathcal{C} e^{\frac{-\tau}{T_{\mathcal{I}}}}$$
 (S9)

where $C = C_1 - C_2$. The T_1 time can thus be estimated via an exponential fit to the normalised data $\mathcal{N}(\tau)$. This method is valid provided the absolute spin contrast $A_0 - A_1$ is independent of τ , which may not be the case in

the presence of charge population relaxation during the dark time τ . Such charge dynamics have been reported in experiments with diamond NV centres [23, 51], but there has been no report of charge relaxation in the V_B^- system. We note that Eq. S9 remains valid even if the MW pulse is imperfect (i.e. it causes only a partial swap of populations) and for arbitrary initial populations, as these effects simply change the values of C_1 and C_2 .

Alternatively, if the background PL is negligible $(I_{\rm B} \ll I_{\rm S})$, then we can normalise the data as follows:

$$\mathcal{N}'(\tau) := \frac{S(\tau) - R(\tau)}{S(\tau) + R(\tau)} = \frac{\mathcal{C}}{2} e^{\frac{-\tau}{T_1}}$$
 (S10)

where we assumed $C_{1,2} \ll 1$. In this case, T_1 can be estimated via an exponential fit to the normalised data $\mathcal{N}'(\tau)$ provided the relative spin contrast C is independent of τ . The latter condition may be expected to hold even in the presence of charge relaxation.

Outside these two scenarios, it is generally not possible to estimate T_1 without knowledge of the functional forms of $I_B(\tau)$, $I_S(\tau)$ and $\mathcal{C}_{1,2}(\tau)$. In our experiments, the measured PL contains a non-negligible background contribution (non V_B^- spin related), as evidenced by the PL spectrum Fig. S1 where the non-irradiated powder emits a significant amount of PL overlapping with the V_B^- emission. We also observed that this background PL tends to increase following a dark time which is seen as a common-mode increase in the raw traces $S, R(\tau)$ [Fig. S3(a)]. Furthermore, adding GdCl₃ whether dry or in solution adds a small but non-negligible background contribution. Therefore, the second normalisation method $\mathcal{N}'(\tau)$ cannot be used here. Instead, we used the first method $\mathcal{N}(\tau)$ as it only assumes that the absolute V_B^- spin contribution to the total PL, precisely the product $I_S\mathcal{C}$, is constant independent of τ .

The normalised data is relatively well fit with a mono-exponential function [Fig. S3(b)], here giving $T_1 = 18 \,\mu\text{s}$. A stretched exponential fit $\exp[-(\tau/T_1)^n]$, often used in NV T_1 sensing experiments [9, 15], returns a similar T_1 value but does not seem to fit the data better (not shown). We thus choose to fit all data with a mono-exponential as to reduce the number of fitting parameters. We note that a small deviation from the exponential behaviour is sometimes observed at small τ values, as can be seen in the example Fig. S3(b). This deviation may be due to a decrease in the sample temperature as τ is increased (see Sec. V) or to residual relaxation effects that extend beyond the $\tau = 0 - 2 \,\mu\text{s}$ window. The variability of this deviation across different experiments adds an uncertainty to the measured T_1 values, which we estimate (e.g. by changing the spacing between τ points in the T_1 curve or restricting the fit to larger τ values) to be about $\pm 10\%$.

C. Effect of finite spin initialisation fidelity

In this section, we develop a simple model to quantify the effect of finite spin initialisation (due to a finite laser pulse duration) on the estimated T_1 time. Indeed, in general insufficient repumping from the laser during a T_1 measurement leads to an apparent decay time T_d that is shorter than the true spin decay time T_1 .

We consider a two-level model corresponding to $|0\rangle$ and the doublet $|\pm 1\rangle$ treated as a single level. When the laser is off, these two levels are coupled by the transition rate k_{01} which mediates spontaneous spin relaxation and defines T_1 as discussed in Sec. IV A, where here the relation between the two is $1/T_1 = 2k_{01}$. Turning the laser on adds a pumping rate k_p which drives the $|\pm 1\rangle \rightarrow |0\rangle$ transition [Fig. S4(a)]. This pumping rate scales with the laser intensity used. We apply this model to calculate the population dynamics during our measurement sequence, which alternates a free decay part $(k_p = 0$, duration τ) and a pumping part $(k_p \neq 0$, duration t_p) where t_p is the laser pulse duration [Fig. S4(b)]. Note, while the model omits the overall photodynamics of the defect (e.g., the intersystem crossing) as well as possible charge dynamics effects, we expect it to provide a useful guide to choose an appropriate pulse duration t_p allowing a faithful estimation of T_1 .

We first treat the two stages of the sequence [A and B, see Fig. S4(b)] separately, defining rate matrices Φ_A and Φ_B and solving the corresponding linear matrix rate equations to determine the time-dependent functions for the populations $\rho_0(t)$ and $\rho_{\pm 1}(t)$:

$$\Phi_{A} = \begin{bmatrix} -k_{01} & k_{01} \\ k_{01} & -k_{01} \end{bmatrix} \qquad \Phi_{B} = \begin{bmatrix} -k_{01} & k_{01} + k_{p} \\ k_{01} & -(k_{01} + k_{p}) \end{bmatrix}
\Rightarrow \begin{cases} \rho_{0,A}(t) = C_{0} + C_{1}e^{-2k_{01}t} \\ \rho_{\pm 1,A}(t) = C_{0} - C_{1}e^{-2k_{01}t} \end{cases} \Rightarrow \begin{cases} \rho_{0,B}(t) = C_{2}\frac{k_{01} + k_{p}}{k_{01}} - C_{3}e^{-(2k_{01} + k_{p})t} \\ \rho_{\pm 1,B}(t) = C_{2} + C_{3}e^{-(2k_{01} + k_{p})t} \end{cases}$$
(S11)

To solve for the coefficients C_n , we first use the fact that the system is closed, such that $\rho_{0,A}(t) + \rho_{\pm 1,A}(t) = \rho_{0,B}(t) + \rho_{\pm 1,B}(t) = 1$. Second, since the sequence is repeated $N \sim 1000$ times, we can apply periodic boundary conditions $\rho_{0,A}(0) = \rho_{0,B}(\tau + t_p)$, combined with the trivial condition $\rho_{0,A}(\tau) = \rho_{0,B}(\tau)$ [see Fig. S4(b)].

We obtain:

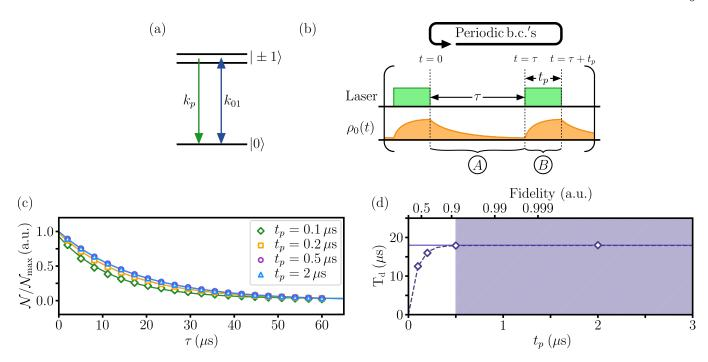


FIG. S4. (a) Simple two-level model used to describe the effect of finite spin initialisation. The two levels are coupled by the two-way transition rate k_{01} defining the spontaneous spin relaxation rate and thus T_1 . When the laser is on there is an additional pumping rate k_p which drives the transition $|\pm 1\rangle \rightarrow |0\rangle$. (b) Schematic representation of the timing for the laser pulses and the effect on the population of the $|0\rangle$ state $\rho_0(t)$. The regions labelled A and B are the areas where we solve the dynamical rate equations by employing the indicated periodic boundary conditions. (c) Simulated relaxation curves plotted as $\mathcal{N}/\mathcal{N}_{\text{max}}$ versus τ for different values of the laser pulse duration t_p . (d) Plot of the decay time T_d versus t_p (bottom axis) and calculated initialisation fidelity (top axis) with T_d being extracted from the curves in (c) by fitting with a mono-exponential. The solid line indicates the nominal T_1 value input into the model ($T_1 = 18 \,\mu$ s) while the dotted line is a separate exponential fit which acts as a guide to the eye which shows how T_d converges on T_1 as t_p is increased. Values for t_p used in experiments were all within the shaded area.

$$\left[\rho_{0,A}(t)\right]_{\text{sig.}} = \frac{1}{2} + \frac{k_p}{2(2k_{01} + k_p)} \left(\frac{e^{-(2k_{01} + k_p)t_p} - 1}{e^{-(2k_{01} + k_p)t_p - 2k_{01}\tau} - 1}\right) e^{-2k_{01}t}$$
(S12)

$$\left[\rho_{\pm 1,A}(t)\right]_{\text{sig.}} = \frac{1}{2} - \frac{k_p}{2(2k_{01} + k_p)} \left(\frac{e^{-(2k_{01} + k_p)t_p} - 1}{e^{-(2k_{01} + k_p)t_p - 2k_{01}\tau} - 1}\right) e^{-2k_{01}t}$$
(S13)

$$\left[\rho_{0,B}(t)\right]_{\text{sig.}} = \frac{k_{01} + k_p}{2k_{01} + k_p} - \frac{k_p}{2(2k_{01} + k_p)} \left(\frac{e^{-2k_{01}\tau} - 1}{e^{-(2k_{01} + k_p)\tau} \left(e^{-(2k_{01} + k_p)t_p - 2k_{01}\tau} - 1\right)}\right) e^{-(2k_{01} + k_p)t}$$
(S14)

$$\left[\rho_{\pm 1,B}(t)\right]_{\text{sig.}} = \frac{k_{01}}{2k_{01} + k_p} + \frac{k_p}{2(2k_{01} + k_p)} \left(\frac{e^{-2k_{01}\tau} - 1}{e^{-(2k_{01} + k_p)\tau} \left(e^{-(2k_{01} + k_p)t_p - 2k_{01}\tau} - 1\right)}\right) e^{-(2k_{01} + k_p)t}$$
(S15)

Note these equations are representative of the 'signal' collection where no MW pulse is applied. Similarly, to obtain equations for the 'reference' measurement, the MW pulse is assumed to perfectly swap the populations of the $|0\rangle$ and $|\pm 1\rangle$ states. For simplicity it is assumed this process is instantaneous and occurs at $t=\tau$. Re-solving for the coefficients with the now new condition $\rho_{0,B}(\tau)=\rho_{\pm 1,A}(\tau)$, new rate equations which describe the reference measurement are obtained, giving:

$$\left[\rho_{0,B}(t)\right]_{\text{ref.}} = \frac{k_{01} + k_p}{2k_{01} + k_p} - \frac{k_p}{2(2k_{01} + k_p)} \left(\frac{e^{-2k_{01}\tau} + 1}{e^{-(2k_{01} + k_p)\tau} \left(e^{-(2k_{01} + k_p)t_p - 2k_{01}\tau} + 1\right)}\right) e^{-(2k_{01} + k_p)t}$$
(S16)

$$\left[\rho_{\pm 1,B}(t)\right]_{\text{ref.}} = \frac{k_{01}}{2k_{01} + k_p} + \frac{k_p}{2(2k_{01} + k_p)} \left(\frac{e^{-2k_{01}\tau} + 1}{e^{-(2k_{01} + k_p)\tau} \left(e^{-(2k_{01} + k_p)t_p - 2k_{01}\tau} + 1\right)}\right) e^{-(2k_{01} + k_p)t}$$
(S17)

Now, we express the PL traces $S(\tau)$ and $R(\tau)$ in accordance with Eq. S4, but here integrating the populations over the laser pulse duration:

$$S(\tau) = I_{\rm B} + \frac{1}{t_p} \int_0^{t_p} dt \left(A_0 \left[\rho_{0,B}(t) \right]_{\rm sig.} + A_1 \left[\rho_{\pm 1,B}(t) \right]_{\rm sig.} \right)$$
 (S18)

$$R(\tau) = I_{\rm B} + \frac{1}{t_p} \int_0^{t_p} dt \left(A_0 \left[\rho_{0,B}(t) \right]_{\rm ref.} + A_1 \left[\rho_{\pm 1,B}(t) \right]_{\rm ref.} \right)$$
 (S19)

Finally, we can express the normalised PL as defined by Eq. S9, i.e. the PL difference $\mathcal{N} = S - R$. This gives:

$$\mathcal{N}(\tau) = \frac{k_p(A_0 - A_1)}{t_p(2k_{01} + k_p)^2} \frac{\left(1 - e^{-(2k_{01} + k_p)t_p}\right)^2}{1 - e^{-2(2k_{01} + k_p)t_p - 4k_{01}\tau}} e^{-2k_{01}\tau}$$
(S20)

To numerically test the influence of the laser pulse duration t_p , in Fig. S4(c) we plot $\mathcal{N}(\tau)$ curves with different values of t_p . The parameters were chosen as $T_1 = 1/2k_{01} = 18\,\mu\mathrm{s}$ and $k_p = 5.1\,\mathrm{MHz}$, the latter corresponding to a typical experimental value, as we will see below. By fitting the curves in Fig. S4(c) with an exponential decay $\exp(-\tau/T_d)$, we can extract the apparent characteristic decay time T_d , which is plotted against t_p in Fig. S4(d). As t_p is increased the value for T_d increases until it reaches a maximal asymptote equal to the true T_1 . Thus, the measured T_d will always be less than T_1 unless $k_p t_p$ is sufficiently large. However, for $t_p \geq 0.5\,\mu\mathrm{s}$ as used experimentally, the relative error $\varepsilon = \frac{T_1 - T_d}{T_1}$ is negligible, $\varepsilon \leq 0.01\%$.

To estimate the experimental pumping rate k_p at a given laser intensity, we use the fact that the maximum PL difference $\mathcal{N}_{\text{max}} = \mathcal{N}(\tau = 0)$ scales with t_p as

$$\mathcal{N}_{\text{max}} = \frac{A_0 - A_1}{k_p t_p} \frac{1 - e^{-k_p t_p}}{1 + e^{-k_p t_p}},\tag{S21}$$

where to obtain a workable expression, we assume that $k_p \gg k_{01}$ which amounts to neglecting spin relaxation during laser pumping, which is a valid assumption as will be justified below. Thus, by measuring \mathcal{N}_{max} as a function of t_p and fitting Eq. S21 to the data, we can estimate k_p for our experimental conditions. An example measurement of \mathcal{N}_{max} vs t_p taken in the conditions of main text Fig. 2 is shown in Fig. S5. Here \mathcal{N}_{max} was taken as the PL difference at $\tau=2\,\mu\text{s}$ rather than at $\tau=0$ to ensure full relaxation to the electronic ground state, but numerically calculating $\mathcal{N}(\tau=2\,\mu\text{s})$ shows the correction is negligible. Fitting Eq. S21 to the data in Fig. S5 gives $k_p=5.1\pm0.5\,\text{MHz}$, which satisfies $k_p\gg k_{01}$ validating the above assumption. This is the value of k_p that was used in the prediction Fig. S4(d).

We can also define an initialisation fidelity

$$\mathcal{F} := 2\rho_{0,B}(t = t_p) - 1 \tag{S22}$$

$$=1-e^{-k_p t_p} \tag{S23}$$

where $\rho_{0,B}(t=t_p)$ is the population at the end of the laser pulse when starting from an unpolarised state, i.e. $\rho_0(t=0)=1/2$. With $k_p=5.1\,\mathrm{MHz}$ as determined before, we obtain $\mathcal{F}=0.93$ for $t_p=0.5\,\mu\mathrm{s}$, for instance. This

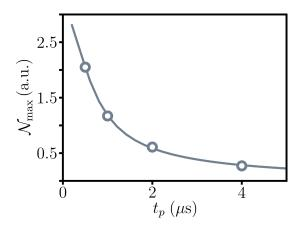


FIG. S5. Experimental data of the spin contrast measured at different laser pulse durations. The data is fit with Eq. S21 in order to extract a value for the pumping rate k_p .

initialisation fidelity directly dictates the relative error ε made in the estimation of T_1 . In all the T_1 measurements presented in the paper, we used a fidelity of $\mathcal{F} > 0.9$, ensuring that the associated error was $\varepsilon < 0.01\%$, well below the statistical noise (i.e. the uncertainty from the fit).

V. T_1 TEMPERATURE DEPENDENCE

As a part of our initial investigation regarding T_1 measurements in our nanopowder samples, we also measured the T_1 dependence on temperature. Measurements were performed using a custom-built wide-field fluorescence microscope which is constructed around a closed-cycle cryostat (Attocube attoDRY1000), described in detail in Ref. [52]. The base temperature of the cryostat is about 5 K, and the sample temperature can be increased to up to room temperature using a heater.

The measurement conditions were similar to the room-temperature measurements as described in Sec. I and III except for the laser power, 50 mW here, resulting in a smaller laser intensity. The powder was dropcast on to a PCB with a MW waveguide in similar fashion to our other samples before being loaded into the cryostat for measurement.

The results of T_1 versus temperature are shown in Fig. S6 over the range $T = 70 - 325 \,\mathrm{K}$. In these measurements, T_1 was found to increase from $T_1 = 15 \pm 3 \,\mu\mathrm{s}$ at room temperature to $T_1 = 160 \pm 30 \,\mu\mathrm{s}$ at $T = 70 \,\mathrm{K}$. We did not measure below 70 K because the required acquisition time became impractically long as T_1 got longer. This temperature dependence indicate that T_1 is governed by a thermally activated process, but further work will be required to elucidate the exact mechanism. For comparison, in Fig. S6 we also plotted the data from Ref. [43] which was obtained with a neutron-irradiated bulk hBN crystal. At low temperatures, the T_1 times we measure in our powders are in general shorter and do not exhibit as strong of an overall dependence on temperature below 250 K. However, at room temperature the T_1 of our powders is similar to the $T_1 \approx 18 \,\mu\mathrm{s}$ value reported in Ref. [43], and can even exceed this value as was the case for powder 1 as reported in the main text.

We also note that the temperature dependence implies that any heating effect during the measurements (caused by laser or MW absorption by the sample) may affect the measured T_1 value. For instance, T_1 will be about 20% shorter if the temperature is raised from 300 K to 320 K, according to Fig. S6. Using pulsed-ODMR spectroscopy and monitoring the shift of the spin resonance frequency ω_0 , it is possible to estimate the temperature experienced by the V_B^- defects [30, 32]. In Fig. 4(a) of the main text, the temperature increase was estimated to be $\approx 70 \,\mathrm{K}$. However, in conditions similar to those of our T_1 measurements, in particular with a minimum delay of $\tau \geq 2 \,\mu\mathrm{s}$ between the laser pulse and the MW probe pulse, we find the heating to be generally less than $\approx 20 \,\mathrm{K}$ above room temperature

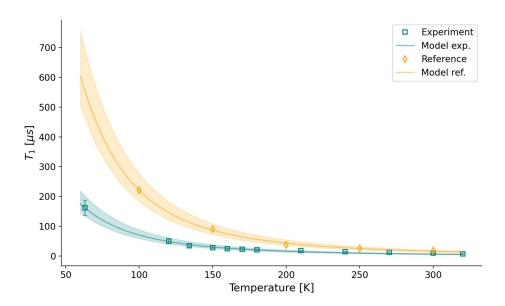


FIG. S6. Temperature dependence of T_1 of powder 2 (green squares) in comparison with the data from Ref. [43] obtained with a neutron-irradiated bulk hBN crystal (orange diamonds). Solid lines are a power law fit, with the shading indicating one standard error.

at $\tau = 2 \,\mu$ s, with further cooling at longer τ . Therefore, T_1 is expected to be shortened by 20% at most as a result of heating, compared to the room-temperature value. This effect is one of the major sources of uncertainty in our experiments, and may explain the variability sometimes observed between T_1 measurements, since the local sample temperature will be sensitive to the specific experimental conditions.

VI. DETERMINING THE EXPECTED T_1 QUENCHING

Here we model the expected contribution to the total relaxation rate from the external paramagnetic ions. As stated in the main text, the total relaxation rate (Γ_1) is the sum of both the intrinsic (Γ_1^{int}) and external magnetic noise (Γ_1^{ext}) contributions. The latter is caused by randomly fluctuating magnetic fields and is thus described by [9, 10]

$$\Gamma_1^{\text{ext}} = 3\gamma_e^2 B_\perp^2 \frac{\tau_c}{1 + \omega_0^2 \tau_c^2} \tag{S24}$$

where γ_e is the electron gyromagnetic ratio, B_{\perp}^2 is the variance in the fluctuating transverse dipolar magnetic field which constitutes the noise source, τ_c is its correlation time, and ω_0 is the resonant frequency of the V_B^- triplet ground state. We can use this equation to model the expected quenching effect by first finding an expression for B_{\perp}^2 . The dipolar field radiated by a spin S_n at a point in space r_n is

$$\mathbf{B}_n = \frac{\mu_0 \gamma_e \hbar}{4\pi r_n^3} \left[\mathbf{S}_n - 3(\mathbf{S}_n \cdot \mathbf{u}_n) \mathbf{u}_n \right], \tag{S25}$$

where $\mathbf{u}_n = \mathbf{r}_n/r_n$. For a fluctuating (paramagnetic) spin, we assume all projections of the spin are equally probable and so take the trace over a purely mixed state described by the density matrix $\rho = \frac{1}{2S+1} \mathbf{1}_{2S+1}$,

$$B_{\perp,n}^2 = \langle B_{x,n}^2 \rangle + \langle B_{y,n}^2 \rangle = \text{Tr}[\rho(B_{x,n}^2 + B_{y,n}^2)] = \left(\frac{\mu_0 \gamma_e \hbar}{4\pi}\right)^2 C_S \frac{2 + \sin^2 \theta_n}{r_n^6}$$
 (S26)

where $C_S = \text{Tr}[\rho S_{i,n}^2] = \frac{1}{2S+1} \sum_{m=-S}^S m^2 = \frac{S(S+1)}{3}$ with i=x,y,z, and θ_n is the angle between the z-axis (V⁻_B quantisation axis) and \mathbf{r}_n . For a slab of hBN with thickness 2d and containing V⁻_B at a depth d [Fig. S7], assuming a

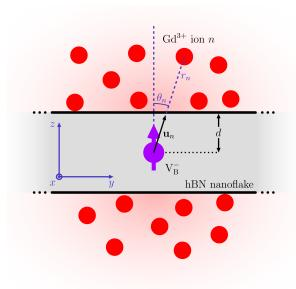


FIG. S7. Schematic representation of the geometry for which the variance B_{\perp}^2 of the transverse magnetic field experienced at the V_B^- from a bath of external paramagnetic spins (Gd³⁺) is derived. The V_B^- is assumed to exist at the centre of a hBN nanoflake with thickness 2d, which is much smaller than the lateral dimensions (i.e. an infinite slab of hBN with finite thickness). We define the principle axis of the V_B^- to be along the z-axis and also describe the locations of the Gd³⁺ spins relative to the centre of the defect. The problem is assumed to be symmetric about the defect in the x and y directions.

density of external spins ρ_{ext} occupying all space external to the slab of hBN, we can obtain the total transverse field by summing over all external paramagnetic ions,

$$B_{\perp}^{2} = \sum_{n} B_{\perp,n}^{2} = \left(\frac{\mu_{0} \gamma_{e} \hbar}{4\pi}\right)^{2} \rho_{\text{ext}} C_{S} \int_{0}^{2\pi} d\phi \int_{0}^{\frac{\pi}{2}} d\theta \sin\theta \int_{\frac{d}{\cos\theta}}^{\infty} dr \frac{2 + \sin^{2}\theta}{r^{4}}$$
 (S27)

$$= \left(\frac{\mu_0 \gamma_e \hbar}{4\pi}\right)^2 \frac{\pi \rho_{\text{ext}} C_S}{3d^3}.$$
 (S28)

In our initial quenching experiment, we assume the solution of GdCl₃ percolates through the hBN powder film and surrounds individual flakes of hBN before evaporation which leaves behind crystalline GdCl₃. The crystal has a density of $4520\,\mathrm{kg\,m^{-3}}$ and molar mass $0.236\,\mathrm{kg\,mol^{-1}}$ giving a Gd³⁺ density of $\rho_\mathrm{ext}=1.03\times10^{28}\,\mathrm{m^{-3}}$ with each Gd³⁺ contributing $S=\frac{7}{2}$. In the optimal case where there is maximal coupling between the noise source and the V_B defect then $\tau_c=\frac{1}{\omega_0}$ with $\omega_0\approx2\pi\times3.45$ GHz. For a flake of thickness $2d=10\,\mathrm{nm}$, and given there is an effectively infinite volume of Gd³⁺ ions on both sides of the flake (thus we double the magnetic noise) we calculate $\Gamma_1^\mathrm{ext}=27\,\mathrm{kHz}$ which approximately matches our experimentally measured value of $30\,\mathrm{kHz}$. We note for this calculation we have chosen an idealised value for the correlation time τ_c of the noise source; however, we have compensated by using a conservative value for the thickness of the hBN flake which is over one standard deviation larger than what the AFM data in Sec. II indicates. If instead we assume the mean thickness of $2d=6\,\mathrm{nm}$, we can relax the optimised choice on τ_c and reduce or increase its value by a factor of ≈ 10 to obtain the same Γ_1^ext , i.e. $\tau_c\approx\frac{10}{\omega_0}$ or $\tau_c\approx\frac{1}{10\omega_0}$. Furthermore this model assumes a single V_B defect located at the middle of a flake which is the worst case scenario in terms of sensitivity. The electron irradiation process should populate a hBN flake with multiple defects distributed throughout and thus would allow us to further relax the conditions on τ_c .